Nonequilibrium Solute Capture in Passivating Oxide Films

Xiao-xiang Yu,[1] Ahmet Gulec,[1] Quentin Sherman,[1] Katie Lutton Cwalina,[2] John R. Scully,[2] John H. Perepezko,[3] Peter W. Voorhees,[1] and Laurence D. Marks[1,*]

[1]*Department of Materials Science and Engineering, Northwestern University, Evanston, Illinois 60208, USA*

[2]*Department of Materials Science and Engineering, University of Virginia, P.O. Box 400745, 395 McCormick Road, Charlottesville, Virginia 22904, USA*

[3]*Department of Materials Science and Engineering, University of Wisconsin-Madison, 1509 University Avenue, Madison, Wisconsin 53706, USA*

(Received 25 July 2018; published 4 October 2018)

We report experimental results on the composition and crystallography of oxides formed on NiCrMo alloys during both high-temperature oxidation and aqueous corrosion experiments. Detailed characterization using transmission electron microscopy and diffraction, aberration-corrected chemical analysis, and atom probe tomography shows unexpected combinations of composition and crystallography, far outside thermodynamic solubility limits. The results are explained using a theory for nonequilibrium solute capture that combines thermodynamic, kinetic, and density functional theory analyses. In this predictive nonequilibrium framework, the composition and crystallography are controlled by the rapidly moving interface. The theoretical framework explains the unusual combinations of composition and crystallography, which we predict will be common for many other systems in oxidation and corrosion, and other solid-state processes involving nonequilibrium moving interfaces.

DOI: 10.1103/PhysRevLett.121.145701

Every metal, with the sole exception of gold, is unstable in air relative to its oxide at room temperature. The only reason they can be used in many applications is because protective oxide films form that limit further oxidation; many metals in aerospace, medical, nuclear, solar, geothermal, and spent nuclear fuel disposal rely on a protective, nanoscale oxide film. Although much of the general science of how the oxides form is known, there are still gaps. Much of our current knowledge is from the mesoscale down to several nanometers, but multiple processes over wide spatial and temporal scales control their nucleation, composition, stability, and structure. Understanding and predicting oxide growth is critically important if we are to move beyond remedial treatment and coating of metallic surfaces or empirical alloy composition selection towards science-guided alloy design. This is becoming increasingly urgent with aging infrastructure in the developed world, the use of metallic alloys in increasingly harsh environments, as well as the ever-increasing costs of failure of corroded components.

We demonstrate here that unusual combinations of structure and chemical composition are a general phenomenon in these oxide films and provide a predictive explanation building upon the well-established science of nonequilibrium interfaces [1], extended to moving oxide-substrate interfaces. The experimental evidence indicates that rather than analyzing the development of these oxides using crystallography, chemical composition, or concepts based upon equilibrium thermodynamics, one has to analyze *both* the crystallography and chemistry, combining these with a nonequilibrium approach.

We use "nonequilibrium" deliberately to denotes a phase, reaction, or process that departs from full equilibrium. At the first level of departure, equilibrium phases are present, but their compositions are not in equilibrium except at the interfaces where there is more rapid diffusion than in the bulk; the interface is in local equilibrium. At the next level of departure, metastable phases are present and the interface is in local equilibrium. The metastable phases can be equilibrium phases with a nonequilibrium composition, or ones absent from the equilibrium phase diagram. In nonequilibrium there is a full breakdown of the local equilibrium approximation in the phases and at the interface, and the oxide composition is a function of the interface velocity. One has to use approaches such as extended irreversible thermodynamics [2] or the nonequilibrium thermodynamics of interfaces [3]. We show here that during corrosion, whether high-temperature oxygen, steam, aqueous, or other, frequently the interfaces move fast compared to the timescale for establishing local equilibrium, and a nonequilibrium approach is needed.

As general background on how these oxide films develop, starting from a clean alloy a thin oxide film develops with a potential gradient across it, as first described by Cabrera and Mott [4]. As the film thickness increases, point defects diffuse across the oxide driven by the chemical potential gradients and electric fields [4–15], until the film thickness becomes large enough that diffusion

controls, as first described by Wagner [16], and expanded upon by others [7,16–22]. In an aqueous environment, the film may never reach this limit due to dissolution at the oxide-electrolyte interface [23,24].

Throughout the existing literature, thermodynamically favored oxide phases are commonly assumed to form [25–28], or phases which are stable in Pourbaix diagrams [29], for instance, pure nickel oxide and chromia for nickel-chromium-based alloys [30–34], often enriched with alloying elements [35–38]. One explanation is that during oxidation the more energetically favored (lowest free-energy) oxides form first [25,39]. As noted by Wagner [18,40] and further developed by Chattopadhyay and Wood [41], free energies do not explain the development of the oxide. Experimentally the initial oxide is sometimes a metastable variant that converts to the thermodynamically stable form with slower kinetics [42–45], suggesting Ostwald's step rule [46–50] where faster growing phases form first. For aqueous films there is extensive x-ray photoelectron spectroscopy (XPS) data [25,51], typically interpreted in terms of the thermodynamically stable oxides. For oxidation, x-ray or electron diffraction [43,52–54] has been widely used to identify the lattice parameters of the phases which are then compared to known oxides.

There are two critical issues with the current literature. The first is interpretation of crystal structures from XPS measurements of local valence states or diffraction experiments. XPS is sensitive to the valence and local coordination, not the crystallographic arrangement of atoms. Hence a spectroscopic signature similar to that of a standard only proves that the local chemical environment is similar. Similarly, a lattice parameter and/or spacings close to a known standard only proves that the atomic arrangement is similar. To rigorously identify a phase one has to simultaneously determine *both* the crystallographic arrangement of the atoms *and* the chemical composition.

The second issue involves approaches to solving the transport equations for oxidation. These have chemical rate equations or some other boundary condition for how atoms cross the interface between the metal and oxide. Such formulations will lead to solute atoms being injected into the oxide; however, there is a physical inconsistency. In both oxidation and aqueous corrosion there is a moving oxidation front that combines point defect migration across the interface and physical motion of the interface. The interface therefore has an effective velocity proportional to the rate of incorporation of alloy atoms as cations in the oxide. As this velocity tends to infinity, a necessary constraint is that the chemical composition of cations in the oxide has to be that of the alloy, A second constraint is that as the interface velocity tends to zero, thermodynamics stable or metastable phases with compositions bounded by thermodynamic solubility limits have to be formed. Valid models have to obey these constraints, which requires a term for exchange of cations across the interface that is missing in conventional formulations.

A nonequilibrium formulation for the moving oxide interfaces correctly includes a velocity dependence. As we will show, the compositions formed can be predicted and calculated using a "nonequilibrium solute capture" framework based solely upon the ratio of the velocity of the interface and an effective velocity for equilibration. Independent of whether the phases formed follow Ostwald's step rule [46–50], or are those of lowest free energy, the composition is *controlled* by the metal-oxide interface velocity.

The systems herein are Ni-Cr-Mo alloys oxidized in air at intermediate temperatures in the range 500–800 °C, as well as the same alloys passivated electrochemically in aqueous environments. While specific details varied with the particular alloys and treatment conditions, we will demonstrate that solute capture during oxide film growth is a general phenomenon. The main experimental tools used are transmission electron microscopy and atom-probe tomography (APT). We have examined bulk samples which were oxidized and then appropriate regions extracted using conventional sample preparation methods, as well as samples first prepared in the appropriate geometry for examination and then oxidized or corroded. More details are provided in Supplemental Material, Sec. I [55].

Independent of whether the oxide formed by dry oxidation or in aqueous conditions, the first product is an oxide with a rocksalt structure ($Fm\bar{3}m$). (We describe the oxides by both the crystallographic space group and chemical composition; both need to be specified.) Similar oxides have been reported in the literature, typically interpreted as nickel oxide since they have similar lattice parameters, with perhaps additional solute metal atoms at low concentrations. From electron diffraction data as well as high-resolution imaging (see Fig. S1 of Supplemental Material [55]) the crystallographic structure is rocksalt ($Fm\bar{3}m$), but examination using both APT and chemical analysis inside electron microscopes (Fig. 1 for an aqueous sample) shows that there is very significant chromium and traces of molybdenum in the $Fm\bar{3}m$ oxide. Ignoring the low molybdenum concentration, the composition of this rocksalt ($Fm\bar{3}m$) structure is $Cr_{1-x}Ni_xO_y$, with $x \sim 0.5$. The oxygen content is approximately $y = 1.25$ at the outer surface and closer to $y = 1$ adjacent to the metal or for very thin oxides. This implies Cr^{3+} at the external surface and Cr^{2+} at the metal-oxide interface. This chromium content is significantly larger than the thermodynamic solubility limit of chromium doping in NiO [56]. According to equilibrium thermodynamics this oxide should phase separate into nearly pure rocksalt NiO ($Fm\bar{3}m$) and corundum Cr_2O_3 ($R\bar{3}c$). It has not, neither during high-temperature oxidation, the aqueous corrosion, nor the days to weeks after sample preparation before examination by electron microscopy or APT.

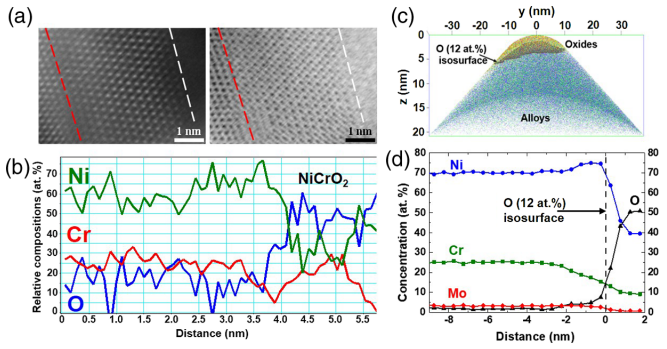

FIG. 1. Chemical data for the oxide on a Ni-22%Cr-6%Mo (wt %) alloy oxidized in $K_2S_2O_8$ and Na_2SO_4. (a) High-angle annular dark field image (left) and annular bright field image (right), with (b) the composition from an electron energy loss line scan. The metal-oxide interface is marked in red, the oxide-vacuum in white. The oxide next to the metal is rocksalt ($Fm\bar{3}m$) of composition $\sim Cr_{0.5}Ni_{0.5}O$. Shown in (c) and (d) are atom-probe tomography results for a tip treated under the same conditions with a 12 at. % isosurface in (c) and a proxigram (compositional line scan) in (d), corrected for oxygen detection efficiency, cross-validating the electron microscopy results.

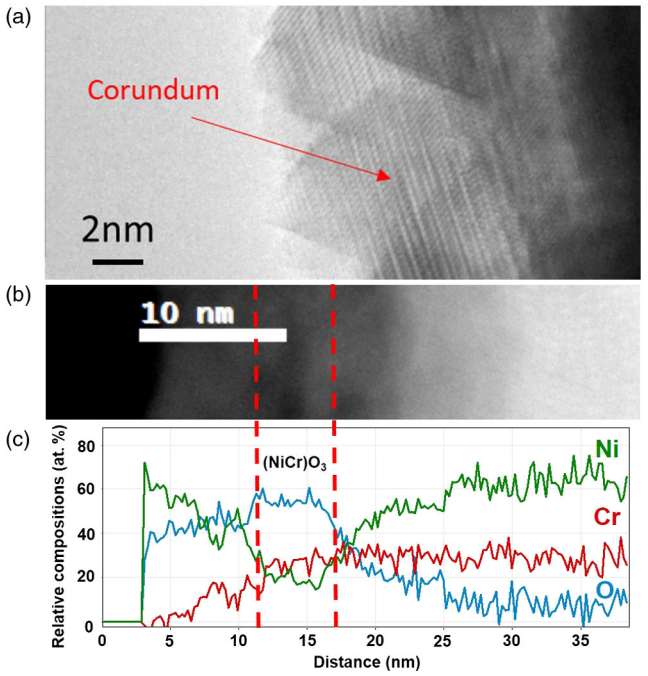

FIG. 2. A Ni-22%Cr-6%Mo (wt %) sample oxidized *in situ* at 700 °C in 1×10^{-4} torr of oxygen, and later analyzed by electron energy loss spectroscopy. (a) A bright field image during *in situ* growth showing fringes characteristic of the corundum ($R\bar{3}c$) structure. (b) A high-angle annular dark field image with the corresponding electron energy loss line scan in (c). The corundum structure adjacent to the metal has a composition of approximately $CrNiO_3$.

The rocksalt phase is not the only structure with a composition far from conventional thermodynamic expectations. For nickel-chromium-iron alloys and nickel-chromium-molybdenum alloys, an oxide with the corundum ($R\bar{3}c$) structure has been reported [25,51,57–60], and assumed to be chromia with perhaps some nickel solute. We can verify the existence of an oxide with a corundum ($R\bar{3}c$) structure; in some cases it is chromia Cr_2O_3 ($R\bar{3}c$), but in others the composition is $Cr_{2-x}Ni_xO_{3-y}$, with $x \sim 1$ (Fig. 2). Here a sample was oxidized *in situ* at 700 °C in 1×10^{-4} torr of oxygen. A metastable $R\bar{3}c$ Ni_2O_3 phase with the corundum ($R\bar{3}c$) crystallography is well established [61], so a metastable corundum $Cr_{2-x}Ni_xO_{3-y}$ ($R\bar{3}c$) is feasible, but far from expectations based upon the published thermodynamic data. [Figure 2(a) is from an *in situ* experiment where $Fm\bar{3}m$ $Cr_{1-x}Ni_xO_y$ was also observed [62].]

Figures 1 and 2 are for relatively thin films, so they could be artifacts of very thin oxide layers or short times. Figure 3 shows results for a sample annealed in oxygen for 24 h at 800 °C, where similar results are found in oxide films more than 300 nm thick. Adjacent to the metal is an approximately 100 nm thick $Cr_{1-x}Ni_xO_{1.5-x/2}$ rocksalt structure ($Fm\bar{3}m$), then over this is nearly pure rocksalt NiO ($Fm\bar{3}m$), with nearly pure corundum Cr_2O_3 ($R\bar{3}c$) at the outer surface. The same sample was examined after being stored for a year in air at room temperature, and had the same overall structure with indications that a small amount of corundum had started to form but rocksalt still dominated for the 100 nm thick region adjacent to the metal-oxide interface; see Fig. S2 in Supplemental Material [55].

While the most definitive evidence is local structural and chemical analysis, *in situ* atomic emission spectroelectrochemistry experiments support the chemical compositions observed in the electron microscopy and APT. These track the metal ions leaving the oxide at the oxide-solution interface versus those oxidized [63] (see Supplemental Material Sec. S3 and Figs. S3 and S4 [55]). The concentrations are quantitatively consistent with those predicted by the solute capture model described later and the results in Fig. 1, namely, rocksalt $Cr_{1-x}Ni_xO_{1.5-x/2}$ (Cr^{3+} and Ni^{2+}) with $x = 0.7$.

The experimental evidence demonstrates the presence of nonequilibrium rocksalt ($Fm\bar{3}m$) and corundum ($R\bar{3}c$) phases with either Ni^{2+} or Ni^{3+} with dominantly Cr^{3+}, possibly Cr^{2+} very close to the metal-oxide interface, and chemical composition far from equilibrium. These are a result of what we call nonequilibrium solute capture at moving oxidation fronts as illustrated in Fig. S5 [55], analogous but different from well-known solute trapping during solidification [1]. Differentiating the two is important. First, in solute trapping atoms add to a moving solidification front; hence, the velocity of the front is coupled to the rate of addition of atoms. In nonequilibrium solute capture, in addition to moving interfaces, either or both vacancies and interstitials are moving. Defining the interface by the location of the oxygen atoms, with the nickel-nickel oxide system the interface can be stationary but still have a net flux of nickel vacancies crossing it.

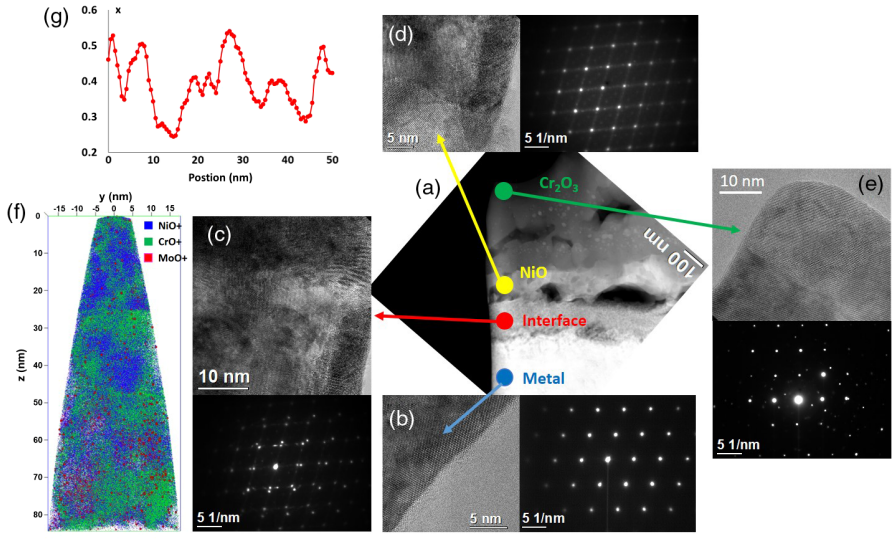

FIG. 3. Results for a Ni-22%Cr-6%Mo (wt %) oxidized at 800 °C for 24 h in air. Shown in (a) is an overview high-angle annular dark field image of a focused ion-beam region cut from the sample. The different layers in (b)–(e) are shown as bright field and diffraction pattern pairs, in (b) of the metal, (c) rocksalt ($Fm\bar{3}m$) $Cr_{1-x}Ni_xO_y$, (d) nickel oxide ($Fm\bar{3}m$), and (e) chromia ($R\bar{3}c$). Shown in (f) is an APT tomogram taken from the interface layer which shows a $Cr_{1-x}Ni_xO_{1.5-x/2}$ rocksalt ($Fm\bar{3}m$) phase, with a one-dimensional composition plot with the metal on the right in (g) of the local chromium fraction on the y axis as a function of position along the x axis.

Secondly, in solute trapping the free energy of the solvent drops whereas that of the solute increases. For instance, with rapid freezing of salt water, the free energy of the water (solvent) drops but that of the retained solute (salt) increases. In contrast, in nonequilibrium solute capture the free energy of both drop.

Two conditions are required for nonequilibrium solute capture. The first is that the free-energy change during formation of the oxide is negative [1]. (See also Supplemental Material Sec. S4 [55].) As shown in Figs. S6 and S7 [55], which combines literature thermodynamic data as well as specific density functional theory results, *all* oxides based upon combinations of Cr^{2+}, Cr^{3+} and Ni^{2+}, Ni^{3+} in *both* rocksalt ($Fm\bar{3}m$) and corundum ($R\bar{3}c$) crystallographies satisfy this first condition. Metastable solid solutions are possible across the whole compositional range. Considering just the rocksalt crystallography of Figs. 1 and 3, the lowest free-energy oxide (per oxygen or metal atom) has the composition Cr_2O_3; i.e., $2/3$ of the cation sites in the cubic unit cell are occupied by chromium atoms. This composition was not observed experimentally because nickel atoms were captured in the rocksalt oxide.

As also shown in Fig. S6 [55], there is the possibility of having Cr^{2+} captured in an $Fm\bar{3}m$ oxide which, rigorously, would be denoted as $Ni_{1-x}Cr_xO$—nickel oxide is the solvent. The microscopy data in Fig. 1 suggest that this occurs at the metal-oxide interface. One can also have Ni^{3+} captured in corundum $R\bar{3}c$, which is $Cr_{1-x}Ni_xO_3$; see Fig. 2.

The second condition is that the interface is moving too fast for equilibrium to be achieved. (See Supplemental Material Sec. S5 [55].) The extent of capture is parametrized by $\beta = v_a/v^D$, where v_a is the velocity of the cations moving into the oxide combining both the physical interface motion and the flux of atoms, which for a planar interface with no adsorption at the interface is $v_a = -c^o v^I + j^o\Omega$, with v^I the physical velocity of the metal-oxide interface, j^o the number of cations crossing the interface per unit area and time (combining vacancy and interstitial contributions), c^o the mole fraction of cations in the oxide, and Ω the atomic volume. The diffusive velocity is $v^D = D_i/a$, where D_i is an interface diffusion coefficient for a Zener exchange of cations and a the hopping distance for exchange between the oxide and metal to equilibrate the composition of the oxide. Nonequilibrium phase compositions form when $\beta \gg 1$ so long as the total free-energy change (condition 1 above) is negative [1].

Turning to the values of β, for planar growth of NiO and using standard values for diffusion constants in the oxide ([64,65] and see Supplemental Material [55]), Fig. 4(a) shows that capture of Ni is expected for a wide range of conditions during high-temperature oxidation (see also Supplemental Material Sec. S5 [55]). It is also probable that $\beta > 1$, during electrochemical passivation, as shown in Fig. 4(b); except for very slow passive aqueous dissolution at $<10^{-7}$ A/cm^2, the effective velocity of the corroding interface using a Faraday's law derived electrochemical interface velocity is faster than the rate of equilibration. This is consistent with our experimental observations.

Our experimental observations and the model for solute capture predict that for many cases of oxidation and almost all aqueous conditions, solute capture for NiCr alloys is the norm, not the exception. The possibility of capture can be predicted using the free energies of the phases and values

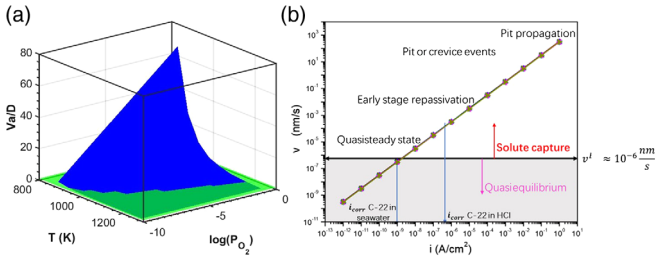

FIG. 4. Kinetic conditions for solute capture, in (a) for oxidation based upon literature diffusion constants and reaction rates as a function of exposure temperature and oxygen partial pressure in atmospheres for an oxide thickness of 5 nm and a hopping distance of 1 nm. The horizontal green plane is $v^a a/D_i = 1$, the blue surface the ratio for different temperatures and oxygen pressures. For a wide range of conditions, oxidation is expected to lead to solute capture, consistent with the experimental results. In (b) a plot of the local electrochemical corrosion current density along x and the velocity of the oxidation front along y for a range of different processes in aqueous corrosion with the approximate diffusion velocity D_i/a marked on the right for $a = 1.0$ nm, assuming a field-affected diffusivity of 10^{-20} cm^2/ sec; again solute capture will be common.

for the interface diffusion constant and hopping distance. Where there are competing solute capture phases, which of these will form for different conditions can in principle be predicted, as briefly outlined in Supplemental Material Sec. S6 [55], which includes Refs. [1,3,62–64,66–108]. Expanded thermodynamic databases along with the model for solute capture open the door to deliberately forming oxides of novel compositions, and thus properties for a given application, for instance, better protection and thus significantly longer lifetimes in service.

To illustrate this, and the distinction of this model from the standard idea of cation injection during oxide growth, we will advance some predictions, with caveats that experimental validation is important. Almost all elements in the first transition metal row can form rocksalt oxides, so we tested using density functional theory calculations the thermodynamics of the comparable rocksalt oxides in the $Sc_{2x/3}Mg_{1-x}O$ and $Al_{2x/3}Mg_{1-x}O$ systems. As shown in Supplemental Material Fig. S8 [55], both lead to metastable solid solutions, so are strong candidates for nonequilibrium solute capture. The free-energy change of a nonequilibrium solute captured rocksalt $A_{1-x}B_xO_y$ can be written as

$$\Delta G_{\mathrm{NSC}} = \Delta G^A_{\mathrm{Oxide}} + \Delta G^B_{\mathrm{Oxide}} + E(\Delta r_{\mathrm{Ion}}, T, \ldots),$$

where the first two terms on the right-hand side are the free energies of formation of the single cation rocksalt oxides and the third is the mixing energy, which will depend strongly upon the difference in the ionic radii Δr_{Ion}. The ionic radii across the first transition row are not that different. Since the free energies of formation of the single cation oxides are all significantly negative, ΔG_{NSC} will almost certainly be negative; solute capture is likely to occur across the whole first transition row.

It can also occur with elements below the first transition metal row. To minimize the strain energy we expect higher valences so the valence and coordination specific ionic radii should be similar. For instance, molybdenum is a known beneficial dopant and has ionic radii of 0.83, 0.79 and 0.75 Å for sixfold 3+, 4+, and 5+ states, respectively, which can be compared to 0.83 for sixfold Ni^{2+} and 0.755 for sixfold Cr^{3+}. Hence, we predict the presence of Mo^{3+} solute captured in rocksalt $Cr_{1-x}Ni_xO_{1.5-x/2}$ and Mo^{4+} or Mo^{5+} in corundum $Cr_{2-x}Ni_xO_3$; higher oxidation states are consistent with the available XPS data.

We suspect solute capture occurs in other solid-fluid or solid-solid chemical reactions, not just the formation of protective oxide films or rapid solidification. If the product is lower in free energy, and the reaction front is moving fast enough, the same science holds independent of whether one is dealing with ceramics, metals, semiconductors, or polymers.

The authors acknowledge support from ONR MURI "Understanding Atomic Scale Structure in Four Dimensions to Design and Control Corrosion Resistant Alloys "through Grant No. N00014-16-1-2280. X.-x. Y. and A. G. performed the oxidation and aqueous treatments of the samples and TEM observations, supervised by L. D. M., with electrochemistry input from K. L. C. and J. R. S. X.-x. Y. performed the APT experiments, supervised by L. D. M. Q. S. performed the solute trapping thermodynamics analysis supervised by P. W. V. with discussions with J. H. P. K. L. C. performed the electrochemical tests supervised by J. R. S. L. D. M. performed the density functional theory calculations. All authors contributed to the writing of the Letter.

*Author to whom correspondence should be addressed.
L-marks@northwestern.edu.

[1] J. C. Baker and J. W. Cahn, Acta Metall. Mater. **17**, 575 (1969).
[2] D. Jou and G. Lebon, *Extended Irreversible Thermodynamics* (Springer, Amsterdam, 2010), p. 483.
[3] J. C. Baker and J. W. Cahn, *Solidification* (American Society for Metals, Metals Park, OH, 1971), p. 23.
[4] N. Cabrera and N. F. Mott, Rep. Prog. Phys. **12**, 163 (1948).
[5] C. Y. Chao, L. F. Lin, and D. D. Macdonald, J. Electrochem. Soc. **128**, 1187 (1981).
[6] L. F. Lin, C. Y. Chao, and D. D. Macdonald, J. Electrochem. Soc. **128**, 1194 (1981).
[7] A. Atkinson, Rev. Mod. Phys. **57**, 437 (1985).
[8] D. D. Macdonald, J. Electrochem. Soc. **139**, 3434 (1992).
[9] C. Chainais-Hillairet and C. Bataillon, Numer. Math. **110**, 1 (2008).

[10] C. Bataillon, F. Bouchon, C. Chainais-Hillairet, C. Desgranges, E. Hoarau, F. Martin, S. Perrin, M. Tupin, and J. Talandier, Electrochim. Acta **55**, 4451 (2010).
[11] D. D. Macdonald, Electrochim. Acta **56**, 1761 (2011).
[12] A. Seyeux, V. Maurice, and P. Marcus, J. Electrochem. Soc. **160**, C189 (2013).
[13] K. Leistner, C. Toulemonde, B. Diawara, A. Seyeux, and P. Marcus, J. Electrochem. Soc. **160**, C197 (2013).
[14] A. Couet, A. T. Motta, and A. Ambard, Corros. Sci. **100**, 73 (2015).
[15] A. Couet, A. T. Motta, A. Ambard, and R. J. Comstock, in *Proceedings of the 18th International Symposium on Zirconium in the Nuclear Industry*, edited by R. J. Comstock and A. T. Motta (ASTM International, Hilton Head Island, SC, 2016), p. 312.
[16] C. Wagner, Z. Phys. Chem., Abt. B **21**, 25 (1933).
[17] C. Wagner, Z. Phys. Chem., Abt. B **32**, 447 (1936).
[18] C. Wagner, J. Electrochem. Soc. **99**, 369 (1952).
[19] L. Himmel, R. F. Mehl, and C. E. Birchenall, Trans. Am. Inst. Min. Metall. Eng. **197**, 827 (1953).
[20] K. R. Lawless, Rep. Prog. Phys. **37**, 231 (1974).
[21] G. R. Wallwork, Rep. Prog. Phys. **39**, 401 (1976).
[22] H. Hindam and D. P. Whittle, Oxid Met. **18**, 245 (1982).
[23] I. Olefjord and B. O. Elfstrom, Corrosion **38**, 46 (1982).
[24] I. Olefjord, B. Brox, and U. Jelvestam, J. Electrochem. Soc. **131**, C299 (1984).
[25] N. Winograd, W. E. Baitinger, J. W. Amy, and J. A. Munarin, Science **184**, 565 (1974).
[26] R. D. Willenbruch, C. R. Clayton, M. Oversluizen, D. Kim, and Y. Lu, Corros. Sci. **31**, 179 (1990).
[27] P. Saltykov, O. Fabrichnaya, J. Golczewski, and F. Aldinger, J. Alloys Compd. **381**, 99 (2004).
[28] B. Ingham, S. C. Hendy, N. J. Laycock, and M. P. Ryan, Electrochem. Solid State Lett. **10**, C57 (2007).
[29] B. Beverskog and I. Puigdomenech, Corrosion **55**, 1077 (1999).
[30] J. E. Croll and G. R. Wallwork, Oxid Met. **4**, 121 (1972).
[31] A. D. Dalvi and D. E. Coates, Oxid Met. **5**, 113 (1972).
[32] J. J. Gilman, Science **306**, 1134 (2004).
[33] S. E. Ziemniak, L. M. Anovitz, R. A. Castelli, and W. D. Porter, J. Chem. Thermodyn. **39**, 1474 (2007).
[34] L. Kaufman, J. H. Perepezko, K. Hildal, J. Farmer, D. Day, N. Yang, and D. Branagan, CALPHAD: Comput. Coupling Phase Diagrams Thermochem. **33**, 89 (2009).
[35] R. Kirchheim, B. Heine, H. Fischmeister, S. Hofmann, H. Knote, and U. Stolz, Corros. Sci. **29**, 899 (1989).
[36] L. Zhang and D. D. Macdonald, Electrochim. Acta **43**, 2661 (1998).
[37] J. E. Castle and K. Asami, Surf. Interface Anal. **36**, 220 (2004).
[38] D. D. Macdonald, Afinidad : organo de la Asociacion de Quimicos del Instituto Quimico de Sarria **62**, 498 (2005).
[39] L. Kjellqvist, M. Selleby, and B. Sundman, CALPHAD: Comput. Coupling Phase Diagrams Thermochem. **32**, 577 (2008).
[40] C. Wagner, J. Electrochem. Soc. **103**, 571 (1956).
[41] B. Chattopadhyay and G. C. Wood, Oxid Met. **2**, 373 (1970).
[42] J. C. Yang, E. Schumann, I. Levin, and M. Ruhle, Acta Mater. **46**, 2195 (1998).
[43] J. Doychak, J. L. Smialek, and T. E. Mitchell, Metall. Trans. A **20**, 499 (1989).
[44] V. K. Tolpygo and D. R. Clarke, Materials at High Temperatures **17**, 59 (2000).
[45] G. C. Rybicki and J. L. Smialek, Oxid Met. **31**, 275 (1989).
[46] W. Ostwald, Z. Phys. Chem. **22U**, 19 (1897).
[47] I. N. Stranski and D. Totomanow, Z. Phys. Chem., Abt. A **163**, 399 (1933).
[48] R. A. Vansanten, J. Phys. Chem. **88**, 5768 (1984).
[49] J. Nyvlt, Cryst. Res. Technol. **30**, 443 (1995).
[50] N. Niekawa and M. Kitamura, Cryst. Eng. Commun. **15**, 6932 (2013).
[51] A. Machet, A. Galtayries, S. Zanna, L. Klein, V. Maurice, P. Jolivet, M. Foucault, P. Combrade, P. Scott, and P. Marcus, Electrochim. Acta **49**, 3957 (2004).
[52] J. Doychak and M. Ruhle, Oxid Met. **31**, 431 (1989).
[53] M. W. Brumm and H. J. Grabke, Corros. Sci. **33**, 1677 (1992).
[54] M. F. Toney, A. J. Davenport, L. J. Oblonsky, M. P. Ryan, and C. M. Vitus, Phys. Rev. Lett. **79**, 4282 (1997).
[55] See Supplemental Material at http://link.aps.org/supplemental/10.1103/PhysRevLett.121.145701 for methods, as well as additional material as described in the text.
[56] C.-H. Chen, M. R. Notis, and D. B. Williams, J. Am. Ceram. Soc. **66**, 566 (1983).
[57] P. Marcus and J. M. Grimal, Corros. Sci. **33**, 805 (1992).
[58] S. E. Ziemniak and M. Hanson, Corros. Sci. **45**, 1595 (2003).
[59] S. E. Ziemniak and M. Hanson, Corros. Sci. **48**, 498 (2006).
[60] J. E. Maslar, W. S. Hurst, W. J. Bowers, J. H. Hendricks, and E. S. Windsor, J. Electrochem. Soc. **156**, C103 (2009).
[61] W. Pies and A. Weiss, in *b1468, II.1.1 Simple Oxides*, edited by K.-H. Hellwege and A. M. Hellwege, Landolt-Börnstein, Group III, Vol. 7B1, Key Element: O. Pt 1 (Springer-Verlag, Berlin, 1975), https://materials.springer.com/lb/docs/sm_lbs_978-3-540-37856-3_31.
[62] X.-x. Yu, A. Gulec, C. M. Andolina, E. J. Zeitchick, K. Gusieva, J. C. Yang, J. R. Scully, J. H. Perepezko, and L. D. Marks, Corrosion **74**, 939 (2018).
[63] K. Lutton, K. Gusieva, N. Ott, N. Birbilis, and J. R. Scully, Electrochem. Comm. **80**, 44 (2017).
[64] W. K. Chen, N. L. Peterson, and L. C. Robinson, J. Phys. Chem. Solids **34**, 705 (1973).
[65] D. L. Douglass, Corros. Sci. **8**, 665 (1968).
[66] M. Pourbaix, *Atlas of Electrochemical Equilibria in Aqueous Solutions* (Pergamon, New York, 1966), Vol. 1.
[67] B. L. Chamberland and W. H. Cloud, J. Appl. Phys. **40**, 434 (1969).
[68] D. S. Walters and G. P. Wirtz, J. Am. Ceram. Soc. **54**, 563 (1971).
[69] M. J. Aziz, J. Appl. Phys. **53**, 1158 (1982).
[70] M. J. Aziz, Appl. Phys. Lett. **43**, 552 (1983).
[71] W. J. Boettinger, S. R. Coriell, and R. F. Sekerka, Mater. Sci. Eng. **65**, 27 (1984).
[72] K. D. Becker and F. Rau, Phys. Chem. Chem. Phys. **91**, 1279 (1987).
[73] M. J. Aziz and T. Kaplan, Acta Metall. Mater. **36**, 2335 (1988).
[74] J. R. Taylor and A. T. Dinsdale, Z. Metall. **81**, 354 (1990).
[75] K. Sujata and T. O. Mason, J. Am. Ceram. Soc. **75**, 557 (1992).

[76] J. P. Hirth, B. Pieraggi, and R. A. Rapp, Acta Metall. Mater. **43**, 1065 (1995).
[77] B. Pieraggi, R. A. Rapp, and J. P. Hirth, Oxid Met. **44**, 63 (1995).
[78] M. E. Gurtin and P. W. Voorhees, Acta Mater. **44**, 235 (1996).
[79] J. P. Perdew, K. Burke, and M. Ernzerhof, Phys. Rev. Lett. **77**, 3865 (1996).
[80] S. L. Sobolev, Phys. Rev. E **55**, 6845 (1997).
[81] N. Kashii, H. Maekawa, and Y. Hinatsu, J. Am. Ceram. Soc. **82**, 1844 (1999).
[82] S. A. T. Redfern, R. J. Harrison, H. S. C. O'Neill, and D. R. R. Wood, Am. Mineral. **84**, 299 (1999).
[83] K. Ogle and S. Weber, J. Electrochem. Soc. **147**, 1770 (2000).
[84] D. Hamm, K. Ogle, C. O. A. Olsson, S. Weber, and D. Landolt, Corros. Sci. **44**, 1443 (2002).
[85] V. A. Kurepin, D. A. Kulik, A. Hiltpold, and M. Nicolet, Paul Scherrer Institute Report No. 02-04, 2002.
[86] P. Novak, J. Kunes, L. Chaput, and W. E. Pickett, Phys. Status Solidi B **243**, 563 (2006).
[87] F. Tran, P. Blaha, K. Schwarz, and P. Novak, Phys. Rev. B **74**, 155108 (2006).
[88] X. Y. Han and B. J. Spencer, J. Appl. Phys. **101**, 084302 (2007).
[89] J. P. Hirth and T. E. Mitchell, Acta Mater. **56**, 5701 (2008).
[90] F. Tran, J. Kunes, P. Novak, P. Blaha, L. D. Marks, and K. Schwarz, Comput. Phys. Commun. **179**, 784 (2008).
[91] M. Asta, C. Beckermann, A. Karma, W. Kurz, R. Napolitano, M. Plapp, G. Purdy, M. Rappaz, and R. Trivedi, Acta Mater. **57**, 941 (2009).
[92] Y. Mishin, M. Asta, and J. Li, Acta Mater. **58**, 1117 (2010).
[93] J. M. Shi and K. D. Becker, Solid State Ionics **181**, 473 (2010).
[94] K. W. Lee and W. E. Pickett, Phys. Rev. B **83**, 180406 (2011).
[95] Y. Yang, H. Humadi, D. Buta, B. B. Laird, D. Sun, J. J. Hoyt, and M. Asta, Phys. Rev. Lett. **107**, 025505 (2011).
[96] M. J. Duarte, J. Klemm, S. O. Klemm, K. J. Mayrhofer, M. Stratmann, S. Borodin, A. H. Romero, M. Madinehei, D. Crespo, J. Serrano, S. S. Gerstl, P. P. Choi, D. Raabe, and F. U. Renner, Science **341**, 372 (2013).
[97] H. Humadi, J. J. Hoyt, and N. Provatas, Phys. Rev. E **87**, 022404 (2013).
[98] P. Kuhn and J. Horbach, Phys. Rev. B **87**, 014105 (2013).
[99] L. D. Marks, J. Chem. Theory Comput. **9**, 2786 (2013).
[100] Y. Qian, H. P. Wu, Y. Z. Liu, J. Lu, R. F. Lu, W. S. Tan, K. M. Deng, C. Y. Xiao, and G. Lu, Solid State Commun. **170**, 24 (2013).
[101] S. L. Sobolev, Mater. Sci. Technol. **31**, 1607 (2015).
[102] S. L. Sobolev, Acta Mater. **93**, 256 (2015).
[103] J. Sun, A. Ruzsinszky, and J. P. Perdew, Phys. Rev. Lett. **115**, 036402 (2015).
[104] S. L. Sobolev, Acta Mater. **116**, 212 (2016).
[105] A. F. Kusmartseva, A. M. Arevalo-Lopez, M. Halder, and J. P. Attfield, J. Magn. Magn. Mater. **443**, 293 (2017).
[106] C. Xu, X. L. Gan, X. C. Meng, S. F. Xiao, H. Q. Deng, X. F. Li, and W. Y. Hu, J. Cryst. Growth **470**, 113 (2017).
[107] T. K. Andersen, S. Cook, G. Wan, H. Hong, L. D. Marks, and D. D. Fong, ACS Appl. Mater. Interfaces **10**, 5949 (2018).
[108] P. Blaha, K. Schwarz, G. K. H. Madsen, D. Kvasnicka, J. Luitz, R. Laskowsji, F. Tran, and L. D. Marks, *An augmented plane wave + local orbitals program for calculating crystal properties* (Technische Universitat Wien, Austria, 2018).